FULL PAPER

Solar Cells

ADVANCED
ENERGY
MATERIALS

www.advenergymat.de

Surface Passivation and Carrier Collection in {110}, {100} and Circular Si Microwire Solar Cells

*Yun Goo Ro, Renjie Chen, Ren Liu, Nan Li, Theodore Williamson, Jinkyoung Yoo, Sangwan Sim, Rohit P. Prasankumar, and Shadi A. Dayeh**

Surface recombination is a major bottleneck for realizing highly efficient micro/nanostructure solar cells. Here, parametric studies of the influence of Si microwire (SiMW) surface-facet orientation (rectangular with flat-facets, {110}, {100} and circular), with a fixed height of 10 μm, diameter (D = 1.5–9.5 μm), and sidewall spacing (S = 2.5–8.5 μm), and mesh-grid density (1–16 mm^{-2}) on recombination and carrier collection in SiMW solar cells with radial p-n junctions are reported. An effective surface passivation layer composed of thin thermally grown silicon dioxide (SiO_2) and silicon nitride (SiN_x) layers is employed. For a fixed D of 1.5 μm, tight SiMW spacing results in improved short-circuit current density (J_{sc} = 30.1 mA cm^{-2}) and sparse arrays result in open-circuit voltages (V_{oc} = 0.552 V) that are similar to those of control Si planar cells. For a fixed S, smaller D results in better light trapping at shorter wavelengths and higher J_{sc} while larger D exhibits better light trapping at larger wavelengths and a higher V_{oc}. With a mesh-grid electrode the power conversion efficiency increases to 15.3%. These results provide insights on the recombination mechanisms in SiMW solar cells and provide general design principles for optimizing their performance.

1. Introduction

Micro/nanostructures provide promising building blocks for thin and flexible Si solar cells owing to their advantage of reduced volume with enhanced light trapping compared to conventional bulk crystalline Si.[1–7] In particular, radial p-n junctions in micro/nanowire solar cells allow lateral carrier separation, which leads to effective collection of photogenerated carriers over a short collection length.[8–10] However, the power conversion efficiency (η) of Si micro/nanowire solar cells is still low compared to conventional thick Si solar cells. Surface recombination is argued to be the dominant carrier collection loss mechanism in micro/nanostructure solar cells due to their large surface-area-to-volume ratio.[11–13] Severe surface recombination loss can compromise the benefits of improved optical absorption in micro/nanostructures and ultimately degrades η. One common strategy to suppress the surface recombination is to apply surface passivation layers that reduce the surface trap density and photogenerated minority carrier recombination at the surface.[14–17] The majority of previous studies on Si micro/nanowire solar cells utilized circular or cylindrical-shaped wires.[18–29] However, the sidewalls of circular or cylindrical Si microwires (SiMWs) contain high-index planes which are prone to more surface states than properly flat-faceted SiMWs.[23] Thus, controlling the micro/nanowire facets on crystal planes that are known to have low interface state densities may help in reducing surface recombination and recovering the promised performance of micro/nanowire solar cells. Here, we devised a new approach toward SiMW solar cells by introducing SiMWs with well-defined sidewall facets known to result in low surface state densities. Solar cells were fabricated with square-shaped and flat-faceted SiMWs that have {110} and {100} sidewalls together with circular-shaped SiMW solar cells, and their electrical properties are compared to understand the effect of facet orientation on surface recombination. The SiMW solar cell performance is also influenced by the array geometrical design parameters (i.e., size, spacing, and height).[21,24,26,28–31] The surface area of SiMWs can be tuned by varying the size and spacing. In order to understand the correlation of design parameters on surface recombination and carrier collection, we carried out a comprehensive study of SiMW solar cell performance as a function of sidewall spacing (S) and diameter (D) for a fixed total surface area and optimized their cell performance. We observed that the SiMW surface facets with different crystal orientations have insignificant influence of solar cell performance compared to the SiMW height, spacing, and mesh electrode density. We decouple the influence of these design parameters on the optical and electrical characteristics of SiMW solar cells.

Y. G. Ro, R. Chen, R. Liu, Prof. S. A. Dayeh
Integrated Electronics and Biointerfaces Laboratory
Department of Electrical and Computer Engineering
University of California San Diego
La Jolla, CA 92093, USA
E-mail: sdayeh@eng.ucsd.edu
Dr. N. Li, Dr. T. Williamson, Dr. J. Yoo, Dr. S. Sim, Dr. R. P. Prasankumar
Los Alamos National Laboratory
Los Alamos, NM 87545, USA
Prof. S. A. Dayeh
Materials Science and Engineering Program and Department
of NanoEngineering
University of California San Diego
La Jolla, CA 92093, USA

ADVANCED
SCIENCE NEWS
www.advancedsciencenews.com

ADVANCED
ENERGY
MATERIALS
www.advenergymat.de

2. Results and Discussion

2.1. Passivation and Crystal Orientation

The collection efficiency of nano and microstructured solar cells with higher surface-area-to-volume ratio than that of planar junction solar cells is degraded by surface recombination of photogenerated minority carriers. It is known that Si {100} surfaces have lower surface state densities compared to {110} and {111} surfaces, particularly when Si is passivated with its natural oxide, SiO_2.[32] By imaging carrier lifetimes on different surfaces, it has been reported that {100} planes passivated with thermal oxide exhibited lower surface recombination velocities compared to that of {111} planes.[33,34] This suggests that SiMW solar cells with crystalline flat facets with a low surface state density can potentially result in low surface recombination velocities and better minority carrier collection efficiencies.

To investigate the facet orientation effects on surface recombination, we patterned our SiMW cell arrays to have three different facets on a single Si (100) substrate (p-type, 0.2–0.4 Ω cm), {110}, {100} flat facets and circular without a well-defined facet for a reference. The alignment of the SiMW arrays in different facet orientations was determined by a substrate etching step using potassium hydroxide (KOH), which is the lowest at {111} planes and leads to pyramidal etch windows that are intercepted with ⟨110⟩ directions.[35] A plasma-enhanced chemical vapor deposited (PECVD) SiN_x layer (200 nm) was used as a hard mask and was patterned by photolithography and reactive ion etching (RIE) of the SiN_x followed by Si anisotropic etching using 30 wt% KOH at 80 °C. After SiN_x mask removal, we aligned our SiMW arrays with {110} facets perpendicular to the exposed ⟨110⟩ directions during the KOH etch step. Arrays that are defined by 45° rotation in mask design with respect to the {110} ones will naturally form with {100} facets (Figure S1, Supporting Information).[35] The fabrication steps of SiMW cells with radial p-n junctions are described in detail in the Experimental Section and are briefly summarized in **Figure 1**a–f. Figure 1g–i are scanning electron microscopy (SEM) images of {110}, {100} and circular-faceted SiMWs after

inductively coupled plasma RIE (ICP-RIE) etching. A thermal oxidation step followed by stripping in buffered oxide etchant (BOE, 6:1) smoothed the rough sidewalls of SiMWs that were induced by the ICP-RIE etching (Figure S2, Supporting Information).[20,25] This is important in reducing the surface defect density that traps photogenerated carriers.[36]

2.1.1. Microwire Solar Cells versus Planar Solar Cells

The measured light and dark $J–V$ characteristics for the devices displayed in Figure 1 are shown in **Figure 2**. The widths (W) and S for {110} and {100} flat-faceted SiMWs were 1.5 μm and 1 μm, 1.5 μm and 1 μm, respectively. The diameter (D) and sidewall spacing (S) of circular SiMWs were 1.7 μm and 1 μm, respectively. The heights of SiMWs were fixed at 10 μm. In addition to different facet orientations, we compare the performances of solar cells without and with a passivation layer. A combination stack of thermally grown SiO_2 and PECVD SiN_x was chosen for the passivation layer because thermal SiO_2 forms a homogeneous layer with the Si surface with low interface state density while the SiN_x layer provides hydrogen passivation and acts as an antireflection coating (ARC).[15,37] The short-circuit current density (J_{sc}), open-circuit voltage (V_{oc}), fill factor (FF), η, dark saturation current density (J_0), and ideality fill factor (n) are listed in **Table 1**. The J_0 and n were determined by linear extrapolation of the dark $J–V$ curve at low forward bias in the range of $V = 0–0.3$ V. The n (1.52–1.73) for all studied cells are lower than 2, indicating the effectiveness of the passivation and the high quality of these SiMW solar cells to serve as a suitable platform to study the effect of surface recombination. For unpassivated devices, we found significant improvements (46–58%) in the J_{sc} of SiMW cells (24.2–26.1 mA cm^{-2}) compared to that of planar ones (16.5 mA cm^{-2}). Consequently, $V_{oc} = k_b T/q \times \ln(J_l/J_0 + 1)$ is consistently larger by 4–5 mV in SiMW cells (0.539–0.540 V) validated through over 100 device runs. Here, k_b is Boltzmann's constant, T is the temperature, q is the fundamental charge constant, and J_l is the light-generated current density. This higher J_{sc} and V_{oc} for unpassivated SiMW
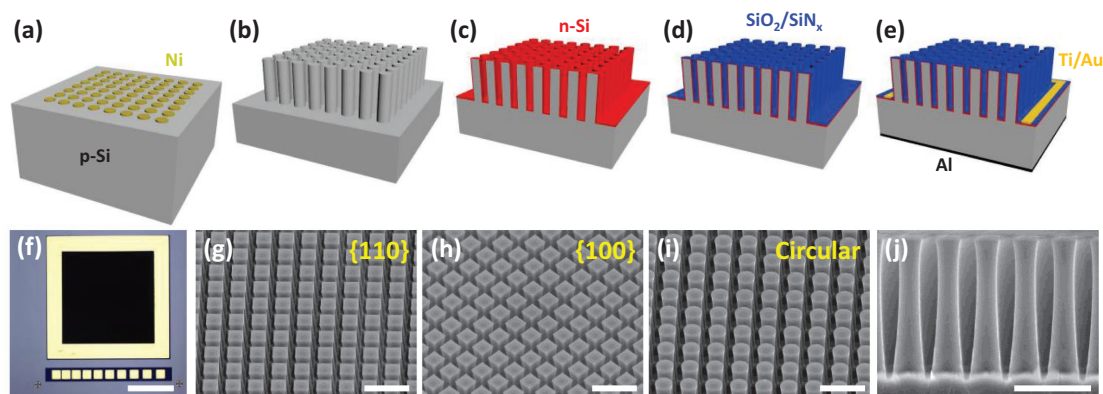

Figure 1. a–e) Schematic illustration of the fabrication process (not to scale). a) Ni dry-etch mask patterning. b) ICP-RIE etching of SiMWs. c) SOD phosphorus doping resulting in radial p-n junction. d) Passivation of SiMW surface with SiO_2/SiN_x layer. e) Mesa etching and patterned top metal electrode deposition; blanket bottom metal contact electrode deposition. f) Top view optical microscopic image of a SiMW solar cell. Scale bar is 500 μm. g–i) 45° view SEM images of 10 μm tall SiMWs with different facets, {110} (width = 1.5 μm, S = 1 μm), {100} (width = 1.5 μm, S = 1 μm) and circular (D = 1.5 μm, S = 1 μm), respectively. Scale bars are 5 μm. j) Cross-sectional SEM image of 10 μm tall SiMWs. Scale bar is 5 μm.
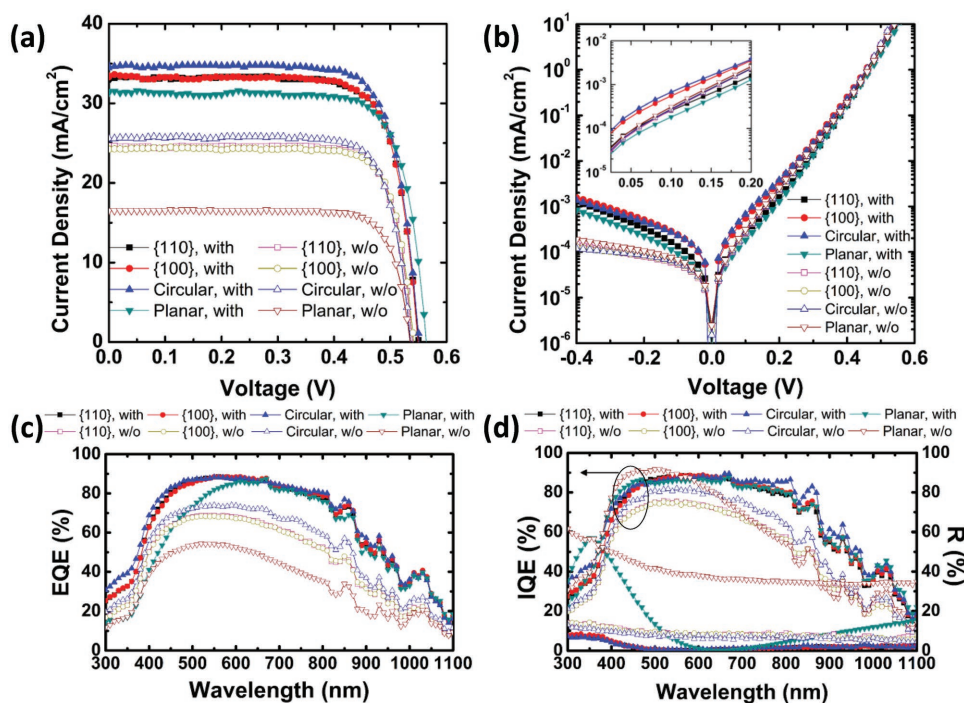
Figure 2. a) Light and b) dark J–V characteristics, c) EQE, d) IQE and reflectance (R) of SiMW solar cell devices with different facet orientations and planar cells without and with a passivation layer (SiO_2/SiN_x, 5/80 nm) (see Figure 1 caption for details of cell topology).

cells compared to unpassivated planar cells is due to superior light absorption. This is deduced by comparing the external quantum efficiency (EQE) in Figure 2c plots to the internal quantum efficiency (IQE) plot in Figure 2d, where the overall EQE for unpassivated planar cells is lower than that of unpassivated SiMW cells but the IQE of planar cells is higher than that for the SiMWs in the 400–600 nm wavelength regime. See the Supporting Information for the procedure of estimation of EQE and IQE. This indicates poor collection efficiency for SiMW cells and that their enhanced absorption characteristics are the dominant contributor for the higher EQE and J_{sc}, and consequently V_{oc}.

When the passivation layer is applied, both J_{sc} and V_{oc} increased due to reduction of surface recombination and increased light absorption assisted by the SiN_x ARC. The J_{sc} for the SiMW cells was ≈6–11% larger than that of planar

cells. This difference is smaller than that for the unpassivated cells. Passivated planar cells exhibited 2% higher V_{oc} but 10.6% lower J_0, than passivated circular SiMW cells likely due to a higher residual surface recombination in the higher surface area SiMWs. This together with a lower ideality factor for the planar cells, that is, sharper forward J–V characteristics, lead to a higher FF for planar cells compared to passivated SiMW cells. It is worth noting that specific contact resistance for all samples was measured with the transmission line method and resulted in a $\rho_{c(unpassivated)} = 7.84 \times 10^{-5}$ Ω cm^2 and $\rho_{c(passivated)} = 2.41 \times 10^{-5}$ Ω cm^2. Secondary ion mass spectrometry (Figure 4) indicated lower phosphorous concentration near the surface for passivated cells compared to unpassivated cells. Therefore, we attribute the lower specific contact resistance for passivated cells due to a better contact/Si interface (lower interface contaminants) with thermally processed samples.

2.1.2. Microwires with and without Facets

To the best of our knowledge, the effect of facet orientation on the SiMW cell performance has not been studied or discussed before. To isolate the influence of surface recombination, we fixed the total surface area (≈7.8 × 10^5 μm^2) of the SiMW cells as well as the S of SiMWs (1 μm) for the {110}, {100} and circular ones (**Table 2**). This deems the volume of the circular SiMWs to be greater than that of flat-faceted SiMWs. The results of this comparison are drawn from Table 1. With surface passivation, the J_{sc} and V_{oc} for {110} flat-faceted SiMW cells increased by 34 and 2%, respectively, and increased by 38 and 2%, respectively, for {100} flat-faceted SiMW cells. The {110} and {100} flat-faceted SiMW cells showed nearly identical

Table 1. Measured solar cell performances of planar and SiMW solar cells with different facet orientations, without and with a surface passivation layer (see Figure 1 caption for details of cell topology).

Facet orientation	J_{sc} [mA cm^{-2}]	V_{oc} [V]	FF [%]	η [%]	J_0 [nA cm^{-2}]	n
{110}, w/o	24.6	0.539	80.8	10.7	200	1.68
{110}, with	33.1	0.550	78.1	14.2	73	1.53
{100}, w/o	24.2	0.540	80.4	10.5	271	1.66
{100}, with	33.3	0.549	77.2	14.1	311	1.71
Circular, w/o	26.1	0.539	81.1	11.4	194	1.67
Circular, with	34.6	0.551	78.6	15.0	284	1.71
Planar, w/o	16.5	0.535	80.9	7.15	271	1.73
Planar, with	31.3	0.563	77.9	13.7	69	1.52

ADVANCED
SCIENCE NEWS
www.advancedsciencenews.com

ADVANCED
ENERGY
MATERIALS
www.advenergymat.de

Table 2. Geometric parameters of {110}, {100} and circular SiMW array solar cells.

Facet type	W or D [μm]	S [μm]	Number of SiMWs	Surface area of device [μm²]	Volume of SiMWs [μm³]
{110}	1.5	1	1.12×10^5	7.76×10^5	2.53×10^6
{100}	1.5	1	1.12×10^5	7.76×10^5	2.53×10^6
Circular	1.7	1	1.27×10^5	7.79×10^5	2.88×10^6

performances in terms of J_{sc} and V_{oc} indicating similar surface recombination effects for both cells. With surface passivation for circular SiMW cells, the J_{sc} and V_{oc} increased by 33 and 2%, respectively. The circular SiMW cells exhibited 4% higher J_{sc} and 0.34% higher V_{oc} than {100} flat-faceted SiMW cells and an $\eta = 15\%$, that is, 1% higher than that of the {100} flat-faceted SiMW cells (Table 1). The higher J_{sc} for circular SiMW cells is attributed to their better light absorption at short wavelengths (higher EQE in Figure 2c and identical IQE in Figure 2d compared to flat-faceted cells) and better collection efficiencies at long wavelengths from 750 to 1000 nm (identical EQE in Figure 2c but higher IQE in Figure 2d compared to flat-faceted cells) that is likely due to their larger cell volume (Table 2) as the total absorption volume increases with SiMWs volume which can efficiently absorb longer wavelength photons.[23,31] To evaluate the effectiveness of the surface passivation layer, we performed ultrafast pump-probe measurements on SiMWs with different facets with and without passivation and investigated their minority carrier lifetime (Figure S3, Supporting Information).[38] For unpassivated SiMWs, the minority carrier lifetimes were longer (≈92 ps for {100} faceted SiMWs, followed by circular and {110} faceted SiMWs (≈61–67 ps). The passivated SiMWs showed extremely slow dynamics with decay times that are well beyond our measurement capabilities (i.e., >1 ns), providing further evidence on the influence of the thermally grown SiO_2 and PECVD grown SiN_x layers on surface passivation, which is consistent with previous results obtained by ours and other groups.[38,39]

While our results agree with earlier works that the SiMW cell performance is enhanced with surface passivation, we did not find that flat-faceted SiMW cells to be advantageous over nonflat SiMW cells. Since the passivated planar cells exhibited lower J_0 and higher V_{oc} than the SiMW cells, this seems to indicate that photogenerated carrier recombination prevails in SiMW cells even with the thermally grown surface oxide passivation. It is possible that this residual recombination blurs the benefits of using one surface facet versus the other or versus the nonflat circular SiMWs. Finally, it is important to note that the metrics presented in Table 1 are reproducible from run to run. Table S1

(Supporting Information) summarizes the results from three different runs in which complete characterization for the different facets and planar reference devices with and without passivation is summarized. We shall note however that there could exist many sources of nonuniformity in the processing of the devices. The most notable ones that we observed in our experiments include the uniformity of the proximity doping across individual samples that needed frequent calibration runs. Another source of nonuniformity includes small variations in the thermal oxide thickness, as further detailed below.

2.1.3. Metrology of Cell Structure and Analysis

To study the structural integrity of the SiMW cells and to understand the differences between SiMW and planar cells, we performed cross-sectional transmission electron microscopy (TEM) analysis on all cell types studied here: {110}, {100} flat-faceted, nonflat circular SiMW cells and a planar cell with passivation (**Figure 3**a–g) and a planar cell without passivation (Figure 3h). First, the TEM images showed no noticeable defects in the SiMW and planar cells (Figure 3 and Figure S4, Supporting Information). Second, despite small variation in the thickness of the thin thermally grown oxide layer at 850 °C between different samples (3–6 nm and nonuniform native oxide layer thickness for unpassivated planar sample), we observed a pronounced difference between the PECVD SiN_x
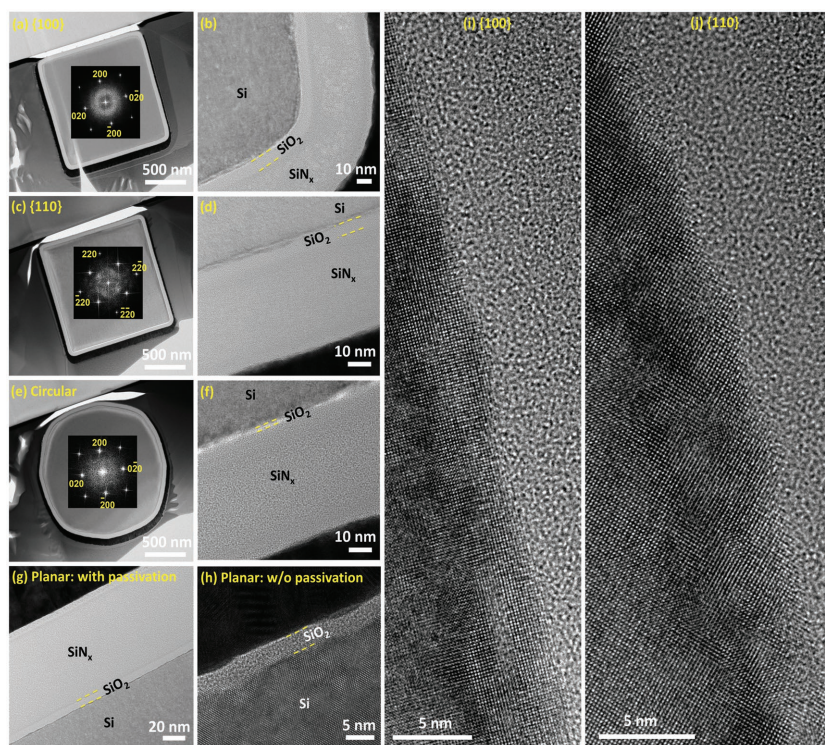

Figure 3. Cross-sectional TEM images. a,b) {100} flat-faceted, c,d) {110} flat-faceted, and e,f) circular SiMWs. Surface passivation has been applied to all SiMW samples in (a)−(f). Insets to (a)−(e) are fast Fourier transforms of higher resolution TEM images taken from the same wires at a zone axis of [100]. g) Planar cell with a passivation layer. h) Planar cell without a passivation layer. i,j) HRTEM images at the side of the cross sections (a) and (b), respectively.

layer thicknesses. The thickness of the SiN$_x$ layer on the sidewalls of the SiMW cells was ≈40 nm whereas on the surface of the planar sample was ≈80 nm, in agreement with optical interferometry measurements (F20, Filmetrics, Inc.) performed on reference planar Si substrates. The shadowing effect of the SiMWs on the PECVD SiN$_x$ deposition in between tightly spaced wires, which is 1 µm for samples investigated with TEM, results in a thinner SiN$_x$ layer on the SiMW sidewalls compared to the nonshadowed planar surface. Thicker SiN$_x$ ARCs result in better absorption at short wavelengths (Figure S5, Supporting Information) and while this effect has been optimized for the planar cells and the top surface of SiMWs, SiMW cells do not cultivate the same absorption benefits on their sidewalls. However, since light trapping effect of SiMWs enhances light absorption at their sidewalls, the optimized thickness of SiN$_x$ ARC at the top surface of SiMWs is more critical.[16] Third, the inset fast Fourier transform (FFT) pattern in Figure 3a–c demonstrated alignment of the facets with the desired crystallographic directions resulting in {100} and {110} facets. For the radial SiMWs, the FFT pattern indicated that the resulting surface facets are of the {210} octahedral type. However, all of these facets are not atomically flat, as illustrated

in the high-resolution TEM (HRTEM) images of Figure 3i,j. This, in addition to the graded diameter (tapering) across the SiMW length suggest imperfect facet orientations and therefore blurred effects on surface recombination and cell performance observed in Figure 2 and Table 1 above. The tapering leads to grading of effective refractive index that is known to enhance optical absorption in 1D nanowires.[40]

To characterize the doping profile and junction depth on the planar and SiMW cells, we performed secondary ion mass spectrometry (SIMS) on planar cells with and without a passivation layer (**Figure 4**a) and a single 1.5 µm wide, 10 µm tall {100} flat-faceted SiMW with and without a passivation layer (Figure 4b). The junction depth (x_j) where the concentration of phosphorus determined from the SIMS profile, and background boron concentration—estimated by a four-point probe measurement prior to doping to be 5.3×10^{16} cm^{-3}—become equal, was estimated to be ≈450 nm for the unpassivated planar cell and ≈570 nm for the passivated planar cell. It should be noted that depth of SIMS profiles starts from the Si surface for the passivated cells and the Si/SiO$_2$ interface, beneath the SiO$_2$/SiN$_x$ passivation layer for the passivated cells. The surface peak concentration of the unpassivated and the passivated
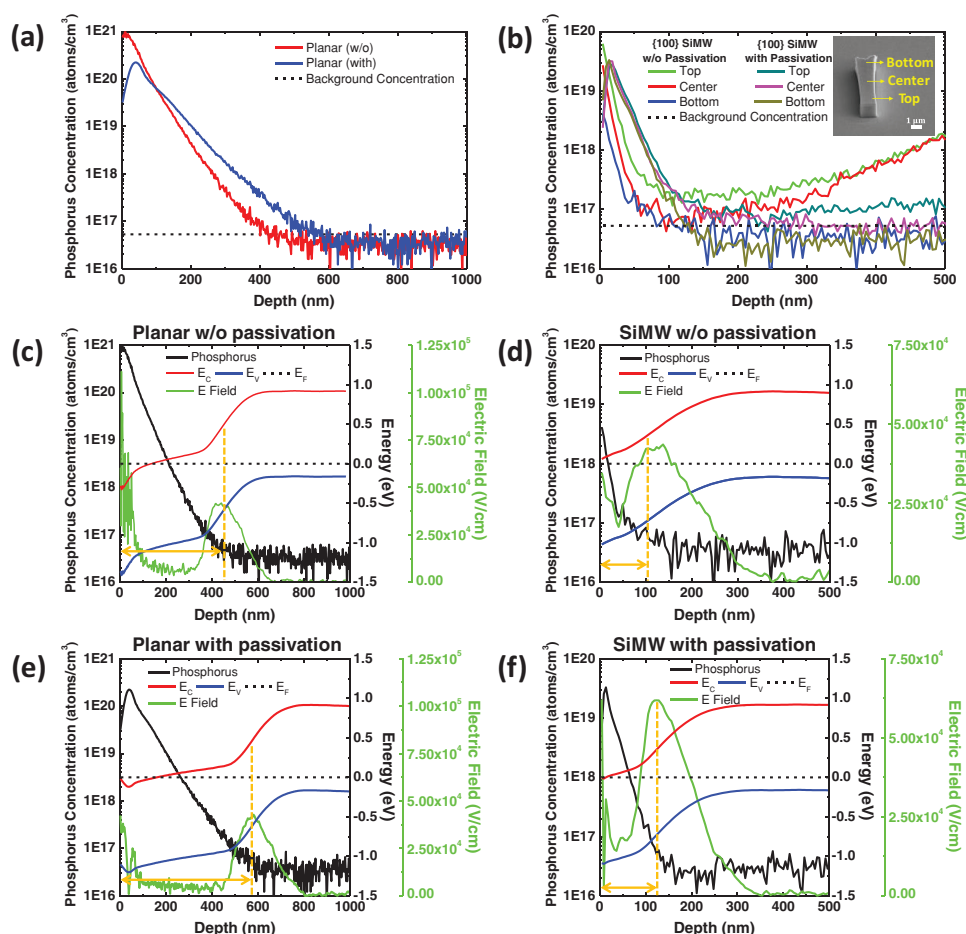

Figure 4. a) Measured SIMS profiles of a planar cell without and with passivation. b) Measured SIMS profiles of a {100} flat-faceted SiMW without and with passivation, measured at top, center, and bottom of the SiMW. Inset is the SEM image of a single {100} flat-faceted SiMW showing locations where the SIMS profiles were measured. Simulated energy band diagram and electric field of a c) planar cell without passivation, d) {100} flat-faceted SiMW (bottom) with passivation, e) planar cell with passivation, and f) {100} flat-faceted SiMW with passivation. x_j indicates junction depth for each cell.

planar cell was measured to be 9.7×10^{20} and 2.2×10^{20} cm^{-3}, respectively. The lower surface peak concentration and the broadening of x_j for the passivated planar cell are attributed to the redistribution of phosphorus dopants during thermal oxidation where phosphorus atoms diffuse to deeper Si during thermal oxidation.[41] For the SiMWs, the SIMS was carried out on three different locations of a single SiMW sidewall: top (1 μm below the tip of SiMW), center (5 μm below the tip of SiMW), and bottom (1 μm above the base of SiMW) as shown in Figure 4b. For SiMWs, we observed larger dopant concentration only at the top region of unpassivated SiMW surface, compared to passivated ones, similar to the planar cell case, while at the center and the bottom region, unpassivated SiMW has lower dopant concentration at the surface. The phosphorus concentration at the surface decreases from the top to the bottom portion of unpassivated SiMWs due to shadowing effects on phosphorous diffusion in between the SiMWs. In contrast to the unpassivated SiMW, the SIMS profiles of the passivated SiMW show nearly identical phosphorus concentration near the surface among three different locations. It is possible that during forming gas annealing at 400 °C, which we performed after passivation layer was applied, phosphorus atoms redistributed in the SiMWs which contributed to a more uniform doping profile.[42] The SIMS profiles at the top and the center region of SiMWs show no obvious p-n junction. This can be attributed to experimental errors induced by the inclination of the small diameter SiMW as it lays down on its side due to a larger base width than tip width and/or procedural errors. Cross-calibration with an ion-implanted reference sample with known dopant profiles and planar cells has been conducted to verify the SIMS results which we concluded to be due to experimental errors during SIMS measurements at the center and tip of the SiMWs. The results exhibited here serve as a qualitative analysis of the differences in the doping profiles within a single SiMW and between SiMW and planar cells. The bottom region of the SiMW exhibited a p-n junction with a shallow depth from the surface of ≈100 nm. To calculate the electric field and energy band-edge profiles for the different cells under consideration, we used Silvaco Atlas simulations to calculate the 1D Poisson's solutions based on the experimentally measured phosphorous dopant profiles (Figure 4c–f). Surface Fermi energy pinning was not accounted for in these simulations. These simulations assumed that all phosphorus dopants are electrically active even though this might not be the case for the very high concentration measured at the planar cells. The energy band diagram, particularly for the planar cells without passivation, resemble an n$^+$-n-p structure with a highly doped surface that results in a strong electric field at the surface that serves as a front surface field layer and reduces surface recombination.[43] This explains higher IQE of planar cells compared to that of SiMW cells at the short wavelength regime for both without and with passivation (Figure 2d) despite the fact that the junction depth and the maximum electric field for charge separation in the cell is closer to the surface for the SiMW cells (x_j = 100–125 nm) than the planar cells (x_j = 450–570 nm). Moreover, the stronger electric field at the surface of the unpassivated planar cell compared to the passivated planar cell explains the poorer blue spectral response of the passivated planar cell than that of the unpassivated one,

which is not the usual case when surface recombination is suppressed by passivation layer.[15] On the contrary, for SiMWs, the electric field is stronger at the surface when SiMWs are passivated compared to that of unpassivated case, which together with reduced surface recombination results in higher IQE at the short wavelength regime of the passivated SiMWs than that of unpassivated SiMWs. Moreover, for high doping concentration (>10^{18} cm^{-3}), Auger recombination limits the photogenerated carrier collection not only at the short wavelength but also at the longer wavelength for the SiMW case because of their efficient absorption of longer wavelength photons.[12] Consequently, lower IQE for unpassivated SiMW cells at longer wavelength (>600 nm) was observed compared to passivated SiMW cells for which the SiN$_x$ passivation layer effectively suppressed the Auger recombination.[15]

2.2. Spacing and Diameter Dependence

To exploit the benefits observed here for absorption and photogenerated carrier collection in SiMW cells, we studied the influence of sidewall spacing (S) and diameter (D) of circular SiMWs in cell arrays that were fabricated side-to-side on the same Si sample. It is natural to expect that the effects of surface recombination will decrease with a lower surface-area-to-volume ratio in SiMW array cells. This can be accomplished by having sparse wire array or increasing the D of SiMWs but such geometries compromise light trapping effects of the SiMWs and the radial charge separation, respectively.[31] Therefore, it is important to find the optimized D and S to have balanced surface recombination, light absorption, and carrier separation that can yield high η for SiMW cells. For the SiMWs with different S, the S of the SiMWs after thermal oxidation and stripping were 2.5, 4.5, 6.5, and 8.5 μm where the D were kept the same as 1.5 μm. For the SiMWs with different D, the D after thermal oxidation and stripping were 1.5, 3.5, 5.5, 7.5, and 9.5 μm where the S were kept the same as 1 μm (Figure S6, Supporting Information). The hole carrier lifetime measurement of the Si substrate (0.11 μs) confirmed that the $D/2$ is smaller than the minority carrier diffusion length (≈15 μm).[8] S and D were defined from the top surface of each SiMW. Circular SiMW arrays were used throughout these studies of the S and D dependence. The height of SiMWs was also fixed at 10 μm.

Tighter S of SiMWs resulted in a higher geometrical fill factor over the active cell area (**Table 3**). On the other hand, the total surface area of the SiMW arrays increased with tighter S and can consequently result in higher surface recombination effects. Furthermore, the increase in surface area corresponds to larger junction area recombination.[14,28] Junction recombination yields increased J_0 which consequently leads to degradation of V_{oc}. This is evidenced by **Figure 5**a,b and Table 3 which show that as the number of the SiMWs decreased with larger S, J_0 decreased and concomitantly V_{oc} increased. The V_{oc} for sparse arrays became similar to that of planar devices (V_{oc} = 0.552 V). The SiMW cell with the tightest S (2.5 μm) exhibited the highest J_{sc} of 30.1 mA cm^{-2} and the best η of 12.7%. Results presented in Table S2 (Supporting Information) measured on six different runs corroborate the above trends.

ADVANCED
SCIENCE NEWS
www.advancedsciencenews.com

ADVANCED
ENERGY
MATERIALS
www.advenergymat.de

Table 3. Measured solar cell performances of SiMW solar cells with different S ($D = 1.5$ μm).

Device ($D = 1.5$ μm)	J_{sc} [mA cm^{-2}]	V_{oc} [V]	FF [%]	η [%]	J_0 [nA cm^{-2}]	n	Relative surface area	Geometric fill factor [%]
$S = 2.5$ μm	30.1	0.545	77.2	12.7	736	1.88	3.63	10.0
$S = 4.5$ μm	29.3	0.550	78.5	12.7	615	1.89	2.22	4.5
$S = 6.5$ μm	28.8	0.552	78.3	12.4	519	1.85	1.71	2.5
$S = 8.5$ μm	27.7	0.552	77.7	11.9	433	1.76	1.44	1.6
Planar	27.0	0.552	77.2	11.5	590	1.89	1.00	–

It is argued that SiMW cells have the advantage of enhancing light absorption through light trapping effects and of efficient carrier separation and collection over short radial distances. Thus, decrease in J_{sc} for sparse arrays (Figure 5c) is attributed to lower number of SiMWs which is evidenced by EQE measurement (Figure 5d). It should be noted that the planar region underneath SiMWs also contributes to J_{sc}. EQE at the short wavelength is largest for the smallest S and decreases as the S becomes larger and exhibit the lowest value for the planar cell. This is due to superior light absorption of SiMWs as evidenced in the reflectance measurement results (Figure 5e). This shows the optical benefit of tighter spaced wires surpassed the disadvantage of surface recombination loss.[26] Planar cells exhibited

the highest IQE at the short wavelength and interestingly, SiMWs with different S resulted in similar IQE spectra. This suggests that the surface recombination due to the large surface area was successfully suppressed by clean wire surface and optimal surface passivation layer (SiO_2/SiN_x). We conclude that the increase in J_0 for arrays with a larger number of SiMWs is more likely due to junction recombination.[14]

We next examined the effect of the D of SiMW on solar cell performance. As the D of SiMW increases, the total surface area of the SiMWs within the 1×1 mm^2 active cell area decreases and becomes close to that of planar cells (**Table 4**). As described above, an increase in the total surface area can increase the possibility of both surface and junction recombination. This is
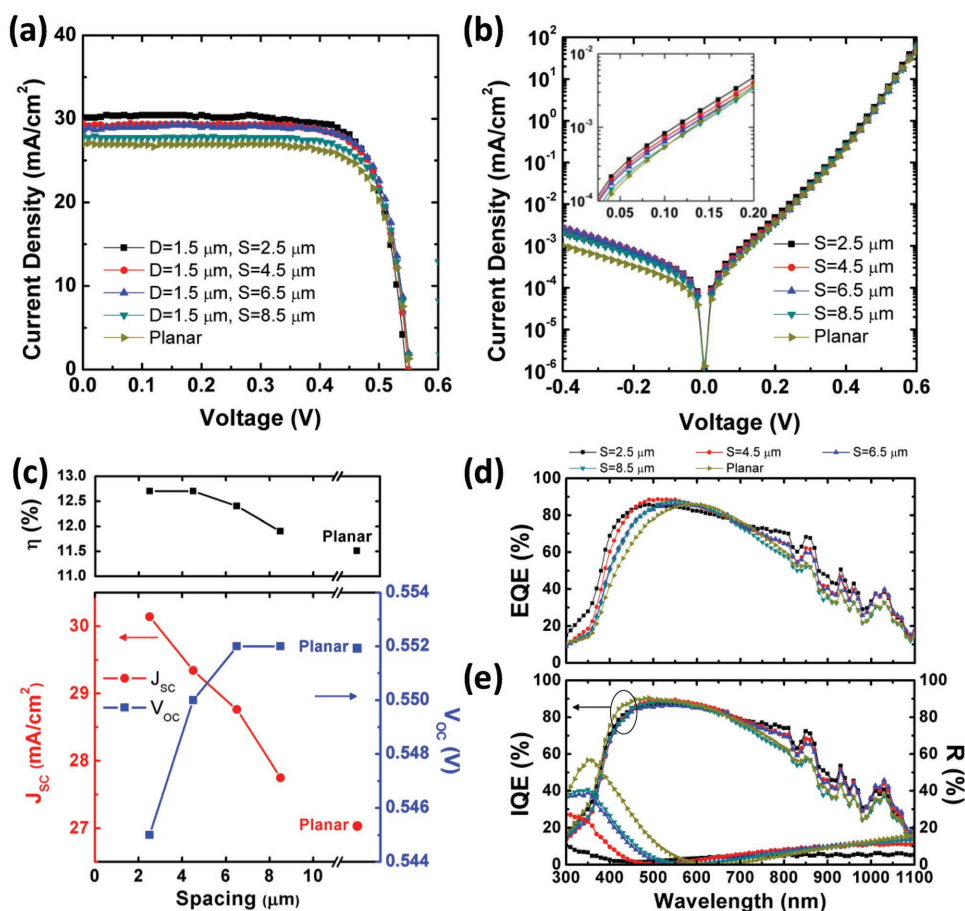

Figure 5. a) Light and b) dark J–V characteristics, c) J_{sc}, V_{oc}, and η dependence on S, d) EQE, e) IQE and R of SiMW solar cell devices with different S ($D = 1.5$ μm).

ADVANCED
SCIENCE NEWS
www.advancedsciencenews.com

ADVANCED
ENERGY
MATERIALS
www.advenergymat.de

Table 4. Measured solar cell performances of SiMW solar cells with different D ($S = 1$ μm).

Device ($S = 1$ μm)	J_{sc} [mA cm^{-2}]	V_{oc} [V]	FF [%]	η [%]	J_0 [nA cm^{-2}]	n	Relative surface area	Geometric fill factor [%]
$D = 1.5$ μm	34.0	0.547	77.2	14.3	160	1.60	8.08	25.8
$D = 3.5$ μm	33.2	0.551	78.0	14.3	107	1.60	6.11	43.4
$D = 5.5$ μm	33.8	0.550	78.1	14.6	82	1.56	4.85	51.4
$D = 7.5$ μm	34.2	0.553	78.4	14.8	77	1.55	4.05	55.4
$D = 9.5$ μm	33.0	0.554	79.0	14.5	75	1.52	3.52	58.2
Planar	31.3	0.563	77.9	13.7	69	1.52	1.00	–

evidenced by the increasing trend in V_{oc} with the D as shown in **Figure 6**a,c. The highest $V_{oc} = 0.554$ V is obtained from the SiMW cells with the largest D (9.5 μm). On the other hand, J_{sc} does not show a clear dependence on D with a fixed S. Ambiguous trend in J_{sc} is attributed to two conflicting factors that determine J_{sc}, light absorption and recombination loss. The SiMW cell with $D = 7.5$ μm and $S = 1$ μm exhibited the best η of 14.8% with $J_{sc} = 34.2$ mA cm^{-2}, $V_{oc} = 0.553$ V, and FF = 78.4%. In order to clarify the D dependence on photovoltaic performance, we evaluated their quantum efficiencies. At the short wavelength, EQE is the highest for the smallest D (1.5 μm) and decreased as the D increases; the largest D (9.5 μm) exhibited the lowest EQE among the SiMW

cells with different D as shown in Figure 6d. From the reflectance measurements shown in Figure 6e, we found that the magnitude of the reflectance at the short wavelength is proportional to the D. When the SiMWs have a large D, the area of the top flat surface of the SiMWs reflects the high-energy photons and lead to a reduced EQE at the short wavelength. For EQEs in the long wavelength range, there is an opposite behavior to the short wavelength region, with the highest EQE at the largest D (9.5 μm) and the lowest EQE at the smallest D (1.5 μm). From these results, we conclude that for the short wavelength, light absorption of SiMWs with smaller D is superior and SiMWs with larger D have better light trapping for long wavelengths. This D dependent spectral response suggests
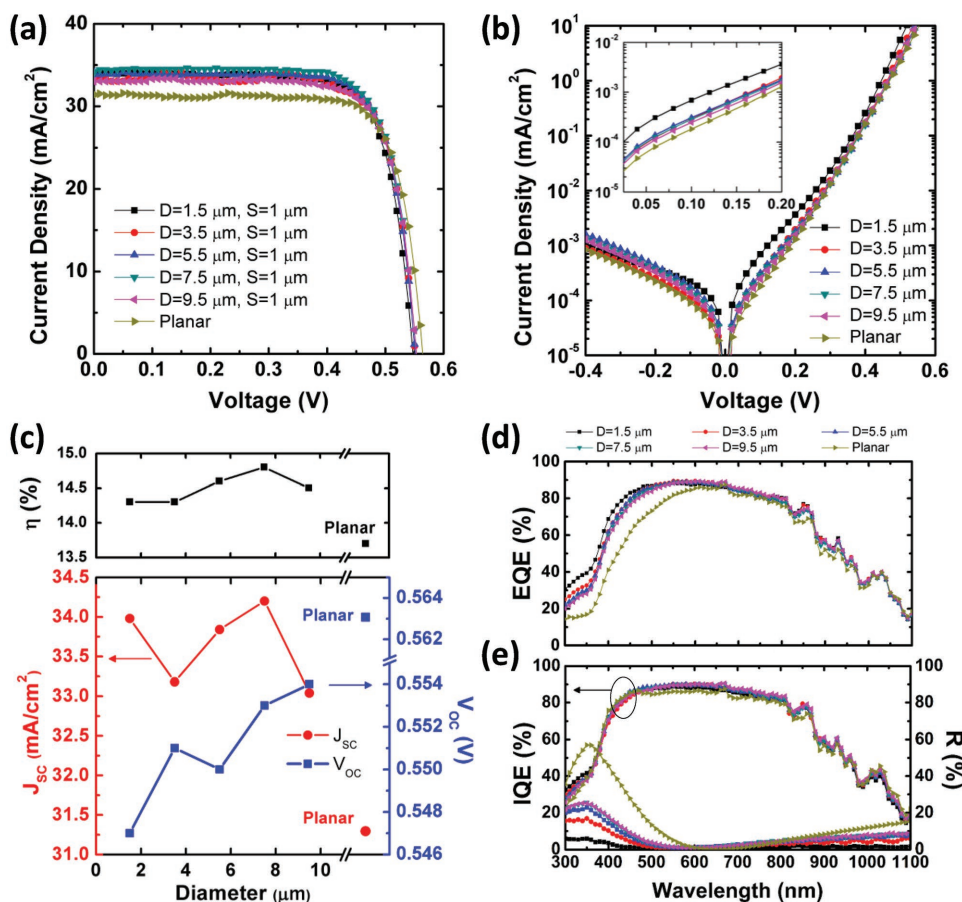

Figure 6. a) Light and b) dark J–V characteristics, c) J_{SC}, V_{OC}, and η dependence on S, d) EQE, e) IQE and R of SiMW solar cell devices with different D ($S = 1$ μm).

that if we combine SiMW arrays with two or more different *D*, we can expect an enhancement in J_{sc}.[44] The similarity in the IQE values at the short wavelength for different *D* indicate that the surface recombination can be suppressed by a surface passivation layer which is in agreement with our discussions above. Results presented in Table S3 (Supporting Information) measured on four different runs corroborate the above trends.

2.3. Contact Design

Finally, our SiMW cell devices do not have a top transparent contact such as transparent conducting oxide over the SiMWs but rather an array-surrounding top contact such that photogenerated carriers need to drift in the thin heavily doped surface n-layer toward the contact. We chose an array-surrounding top contact in order to avoid potential problems of transparent contacts such as their low transmittance at the visible light region[45] or the presence of interfacial defects between these contacts and Si.[46] To reduce the series resistance

encountered in the n-layer of the cell, we applied mesh-type top contact electrodes with different spacings on SiMW cells as displayed in **Figure 7**a–d. Mesh electrodes provide shorter carrier path length which helps in lowering the probability of carrier recombination and thus leads to efficient charge collection.[45,47] The mesh electrodes line width was 20 µm and the mesh side-to-side spacings were for a 2 × 2 mesh, 235 µm, a 3 × 3 mesh, 320 µm, and for a 4 × 4 mesh, 490 µm, where the side-to-side spacing and width of the single electrode without a mesh was 980 and 160 µm, respectively. Here, the *D*, *S*, and height of the SiMWs were 1.5 µm, 1 µm, and 10 µm, respectively, for all meshes. It is worth noting that the metal electrodes were deposited at the bottom part of the SiMWs as shown in Figure 7e to minimize the carrier path length. The light *J*–*V* characteristics and J_{sc}, V_{oc}, and η dependence are displayed in Figure 7f,g. We found a clear increase in J_{sc}, V_{oc}, and FF when the spacing of mesh electrodes became tighter and correspondingly the η. The SiMW cell with the smallest electrode side-to-side spacing (235 µm) showed the highest J_{sc} of 35.2 mA cm⁻², V_{oc} of 0.550 V, and FF of 79.1%, resulting in the best η of 15.3%
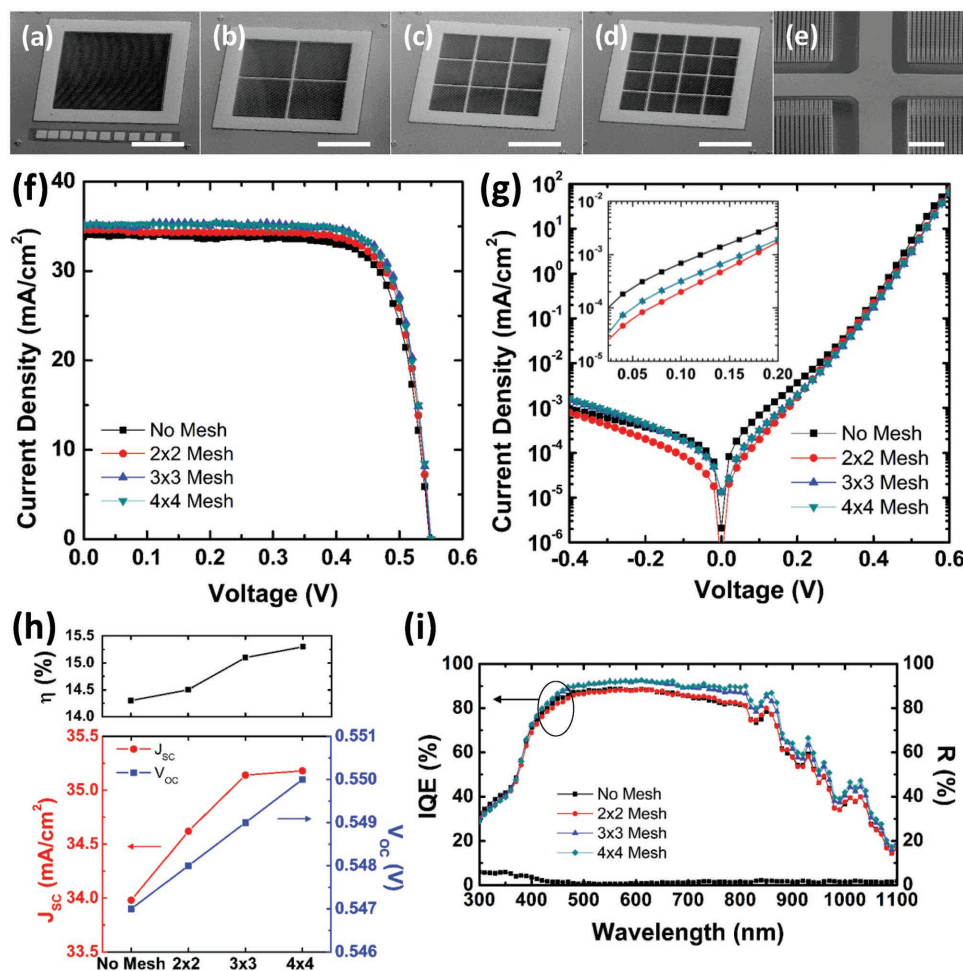

Figure 7. a–d) Overview SEM images (45° view) of SiMW solar cell devices surrounded by Ti/Au contact pads. The *D* and *S* of SiMWs are 1.5 µm and 1 µm, respectively. The side-to-side spacing between adjacent electrodes is a) No mesh: 980 µm, b) 2 × 2 mesh: 490 µm, c) 3 × 3 mesh: 320 µm, and d) 4 × 4 mesh: 235 µm. Scale bars are 500 µm. e) A magnified SEM image (45° view) showing mesh-design top contact electrode and SiMWs. Scale bar is 20 µm. f) Light and g) dark *J*–*V* characteristics, h) J_{sc}, V_{oc}, and η dependence on spacing of electrodes, and i) IQE and *R* of SiMW solar cell devices with different top electrodes.

Table 5. Measured SiMW solar cell performance with different top contact designs ($D = 1.5$ μm, $S = 1$ μm).

Device	Spacing of adjacent electrodes [μm]	J_{sc} [mA cm^{-2}]	V_{oc} [V]	FF [%]	η [%]	J_0 [nA cm^{-2}]	n	R_S [Ω cm^2]
No mesh	980	34.0	0.547	77.2	14.3	160	1.60	1.06
2×2	490	34.6	0.548	77.7	14.7	108	1.55	0.98
3×3	320	35.1	0.549	78.4	15.1	90	1.56	0.97
4×4	235	35.2	0.550	79.1	15.3	88	1.54	0.96

among the devices reported in this work. This mesh spacing dependence is also found in J_0, where J_0 decreased at the same time with spacing of mesh electrode (**Table 5**).

These results indicate that a shorter carrier path length results in reduction of series resistance (Table 5) and assists in efficient carrier collection.[47] Higher IQEs for tighter electrode spacing in overall wavelength region (Figure 7i) indicate that smaller spacing clearly diminished the carrier collection losses. It is notable that this enhancement in IQE at long wavelengths with a tighter electrode design is a manifestation of higher absorption in SiMWs at long wavelengths compared to planar cells where electrode spacing effects at long wavelengths are not significant. Results presented in Table S4 (Supporting Information) measured on three different runs corroborate the above trends.

3. Conclusion

In summary, we performed an experimental parametric study on the effects of surface recombination and array geometry on the detailed performance of SiMW solar cells. Our results showed that with optimal surface passivation, surface recombination can be suppressed and have the advantage of enhanced light absorption from antireflective coating. SiMWs with different surface facets did not result in improved cell performance. Our results suggest that geometrical parameters of SiMWs strongly affect the device performances, especially in dark saturation current and light absorption. We found that for different S and D of SiMWs, the total surface area of SiMWs is reduced, there is an enhancement in V_{oc} which is compromised with lower light absorption. Moreover, carrier recombination loss can be reduced by applying mesh-type electrode that provides short carrier path length.

4. Experimental Section

Fabrication of Vertical SiMW Solar Cells with Radial p-n Junctions: 275 μm thick single crystalline p-type Si(100) wafers (boron doped, 0.2–0.4 Ω cm) were used for this work. The optimal substrate doping density was calibrated in reference planar cells (Figure S7, Table S5, Supporting Information). 200 nm thick Ni arrays were patterned as dry etch masks within an area of 1×1 mm^2 by photo or electron-beam lithography. 10 μm tall vertical SiMWs were etched by ICP-RIE with SF$_6$ and C$_4$F$_8$ gases. After Ni etch masks were removed by a commercial Ni etchant solution (Nickel Etchant TFB, Transene), oxygen plasma clean and Piranha cleaning (H$_2$SO$_4$:H$_2$O$_2$ = 3:1) were performed to remove organic residues from dry etching followed by the standard Radio Corporation of America (RCA) cleaning. Thermal oxidation at 1100 °C for 1.5 h (t_{SiO2} = 120 nm) and 6:1 BOE strip was applied to reduce the sidewall roughness induced by ICP-RIE etching.[20,25] Radial p-n junction was formed by spin-on-doping

(SOD) method in rapid thermal annealing furnace. Prior to doping, SiMW arrays were prepared by the standard RCA cleaning to ensure clean surface. Phosphorus SOD source (P509, Filmtronics, Inc.) was spun-cast on a dummy Si wafer and cured at 200 °C for 15 min to evaporate excess solvent. Then the dummy wafer was placed on quartz spacers within 250 μm from SiMW arrays and annealed at 950 °C for 10 s in N$_2$ ambient followed by postdiffusion cleaning in 6:1 BOE to remove SOD residues. Different annealing times and temperatures for different emitter doping layers were also calibrated for every new bottle of SOD dopant (Table S6, Supporting Information) to optimize doping parameters that yield the best solar cell performance. The surface of the formed p-n junctions was then passivated with a thin (<10 nm) thermally grown SiO$_2$ layer and a PECVD SiN$_x$ layer (80 nm); the SiN$_x$ layer also served as an ARC. The optimal thickness of this layer was calculated to be 80 nm (Figure S5, Supporting Information). The actual thicknesses of SiO$_2$ and SiN$_x$ layer were measured by a spectrometer (F20, Filmetrics, Inc.) on planar cells. Annealing in Forming gas (H$_2$/N$_2$ 5%/95%) at 400 °C was then performed for 30 min to terminate the dangling bonds at the interface between Si and the passivation layer and in the nitride passivation layer.[15] The SiMW arrays were covered by photoresist and Si dry etching of mesa structures for electrical isolation then followed after which the photoresist was stripped away. For the devices with passivation layers, SiO$_2$ and SiN$_x$ were selectively removed for the area where top contact electrode will be deposited. Ti/Au (50/200 nm) was deposited on the n-doped layer as a top ohmic contact and 100 nm of Al was deposited at the backside of p-type substrate for a rear ohmic contact. It should be noted that each set of SiMWs that were used for performance comparison were fabricated on a single wafer where each wafer which also had a planar cell without SiMWs for a reference.

The morphologies of SiMWs were characterized by SEM and TEM. Thin slices of SiMW cross sections were prepared by an FEI Nova 600 Nanolab FIB tool. The TEM characterization was performed in an FEI Titan 80-300 at 300 keV. The TEM studies were performed at the Center for Integrated Nanotechnologies at Los Alamos National Laboratory. The SIMS depth profiles of SiMW and planar cells were recorded by a CAMECA NanoSIMS 50L at Caltech Microanalysis Center. The carrier lifetime of the Si wafer was recorded by quasi-steady-state photoconductance lifetime measurement (WCT-120, Sinton Instruments) with iodine passivation. The minority carrier lifetime of SiMWs was measured by ultrafast pump-probe measurement at the Center for Integrated Nanotechnologies at Los Alamos National Laboratory.

Device Characterization: The photovoltaic performances were measured under dark and light (AM 1.5G) conditions using a solar simulator (67005, Oriel) where 1 Sun (100 mW cm^{-2}) was calibrated using a National Renewable Energy Laboratory (NREL) calibrated reference photovoltaic cell (PV measurements, Inc.). The *J*–*V* characteristics were measured using a potentiostat (DY2300, Digi-Ivy, Inc.). For spectral photoresponse in 300–1100 nm wavelength range, a monochromator (Cornerstone 260, Oriel) equipped with a solar simulator was used and spectral reflectance measurement was carried out using a spectrometer (F40-UV, Filmetrics, Inc.).

Supporting Information

Supporting Information is available from the Wiley Online Library or from the author.

Acknowledgements

Conflict of Interest

The authors declare no conflict of interest.

Keywords

[1] S. Mokkapati, K. Catchpole, *J. Appl. Phys.* **2012**, *112*, 101101.
[2] K. X. Wang, Z. Yu, V. Liu, Y. Cui, S. Fan, *Nano Lett.* **2012**, *12*, 1616.
[3] S. Jeong, M. D. McGehee, Y. Cui, *Nat. Commun.* **2013**, *4*, 2950.
[4] S.-M. Lee, R. Biswas, W. Li, D. Kang, L. Chan, J. Yoon, *ACS Nano* **2014**, *8*, 10507.
[5] M. S. Branham, W. C. Hsu, S. Yerci, J. Loomis, S. V. Boriskina, B. R. Hoard, S. E. Han, G. Chen, *Adv. Mater.* **2015**, *27*, 2182.
[6] K. Lee, I. Hwang, N. Kim, D. Choi, H.-D. Um, S. Kim, K. Seo, *Nanoscale* **2016**, *8*, 14473.
[7] I. Hwang, H.-D. Um, B.-S. Kim, M. Wober, K. Seo, *Energy Environ. Sci.* **2018**, *11*, 641.
[8] B. M. Kayes, H. A. Atwater, N. S. Lewis, *J. Appl. Phys.* **2005**, *97*, 114302.
[9] L. Hu, G. Chen, *Nano Lett.* **2007**, *7*, 3249.
[10] M. D. Kelzenberg, S. W. Boettcher, J. A. Petykiewicz, D. B. Turner-Evans, M. C. Putnam, E. L. Warren, J. M. Spurgeon, R. M. Briggs, N. S. Lewis, H. A. Atwater, *Nat. Mater.* **2010**, *9*, 239.
[11] S. Yu, F. Roemer, B. Witzigmann, *J. Photonics Energy* **2012**, *2*, 028002.
[12] J. Oh, H.-C. Yuan, H. M. Branz, *Nat. Nanotechnol.* **2012**, *7*, 743.
[13] Y. Da, Y. Xuan, *Opt. Express* **2013**, *21*, A1065.
[14] D. R. Kim, C. H. Lee, P. M. Rao, I. S. Cho, X. Zheng, *Nano Lett.* **2011**, *11*, 2704.
[15] X. Lin, X. Hua, Z. Huang, W. Shen, *Nanotechnology* **2013**, *24*, 235402.
[16] W. Vijselaar, R. Elbersen, R. M. Tiggelaar, H. Gardeniers, J. Huskens, *Adv. Energy Mater.* **2017**, *7*, 1601497.
[17] R. Liu, J. Wang, T. Sun, M. Wang, C. Wu, H. Zou, T. Song, X. Zhang, S.-T. Lee, Z. L. Wang, *Nano Lett.* **2017**, *17*, 4240.
[18] M. C. Putnam, S. W. Boettcher, M. D. Kelzenberg, D. B. Turner-Evans, J. M. Spurgeon, E. L. Warren, R. M. Briggs, N. S. Lewis, H. A. Atwater, *Energy Environ. Sci.* **2010**, *3*, 1037.
[19] Y. Lu, A. Lal, *Nano Lett.* **2010**, *10*, 4651.
[20] H. P. Yoon, Y. A. Yuwen, C. E. Kendrick, G. D. Barber, N. J. Podraza, J. M. Redwing, T. E. Mallouk, C. R. Wronski, T. S. Mayer, *Appl. Phys. Lett.* **2010**, *96*, 213503.
[21] O. Gunawan, K. Wang, B. Fallahazad, Y. Zhang, E. Tutuc, S. Guha, *Prog. Photovolt.: Res. Appl.* **2011**, *19*, 307.
[22] M. Gharghi, E. Fathi, B. Kante, S. Sivoththaman, X. Zhang, *Nano Lett.* **2012**, *12*, 6278.
[23] A. D. Mallorqui, F. Epple, D. Fan, O. Demichel, A. Fontcuberta, I. Morral, *Phys. Status Solidi A* **2012**, *209*, 1588.
[24] J. C. Shin, D. Chanda, W. Chern, K. J. Yu, J. A. Rogers, X. Li, *IEEE J. Photovolt.* **2012**, *2*, 129.
[25] J. Yoo, S. A. Dayeh, W. Tang, S. Picraux, *Appl. Phys. Lett.* **2013**, *102*, 093113.
[26] H. Kim, J. Kim, E. Lee, D.-W. Kim, J.-H. Yun, J. Yi, *Appl. Phys. Lett.* **2013**, *102*, 193904.
[27] K. Seo, Y. J. Yu, P. Duane, W. Zhu, H. Park, M. Wober, K. B. Crozier, *ACS Nano* **2013**, *7*, 5539.
[28] R. Elbersen, W. Vijselaar, R. M. Tiggelaar, H. Gardeniers, J. Huskens, *Adv. Energy Mater.* **2016**, *6*, 1501728.
[29] H.-S. Kim, D. B. Patel, H. Kim, M. Patel, K. R. Chauhan, W. Park, J. Kim, *Sol. Energy Mater. Sol. Cells* **2017**, *164*, 7.
[30] F. Voigt, T. Stelzner, S. Christiansen, *Prog. Photovolt.: Res. Appl.* **2013**, *21*, 1567.
[31] J. Yoo, B.-M. Nguyen, I. H. Campbell, S. A. Dayeh, P. Schuele, D. Evans, S. T. Picraux, *ACS Nano* **2015**, *9*, 5154.
[32] S. M. Sze, K. K. Ng, *Physics of Semiconductor Devices*, Wiley, New York **2006**.
[33] S. C. Baker-Finch, K. R. McIntosh, *IEEE J. Photovolt.* **2011**, *1*, 59.
[34] H. C. Sio, T. K. Chong, S. R. Surve, K. J. Weber, D. H. Macdonald, *IEEE J. Photovolt.* **2016**, *6*, 412.
[35] G. Ensell, *Sens. Actuators, A* **1996**, *53*, 345.
[36] T. G. Chen, P. Yu, S. W. Chen, F. Y. Chang, B. Y. Huang, Y. C. Cheng, J. C. Hsiao, C. K. Li, Y. R. Wu, *Prog. Photovolt.: Res. Appl.* **2014**, *22*, 452.
[37] J. Schmidt, M. Kerr, A. Cuevas, *Semicond. Sci. Technol.* **2001**, *16*, 164.
[38] M. Seo, J. Yoo, S. Dayeh, S. Picraux, A. Taylor, R. Prasankumar, *Nano Lett.* **2012**, *12*, 6334.
[39] M. M. Gabriel, J. R. Kirschbrown, J. D. Christesen, C. W. Pinion, D. F. Zigler, E. M. Grumstrup, B. P. Mehl, E. E. Cating, J. F. Cahoon, J. M. Papanikolas, *Nano Lett.* **2013**, *13*, 1336.
[40] J. Zhu, Z. Yu, G. F. Burkhard, C.-M. Hsu, S. T. Connor, Y. Xu, Q. Wang, M. McGehee, S. Fan, Y. Cui, *Nano Lett.* **2009**, *9*, 279.
[41] S. Peters, C. Ballif, D. Borchert, R. Schindler, W. Warta, G. Willeke, *Semicond. Sci. Technol.* **2002**, *17*, 677.
[42] E. Koren, J. Hyun, U. Givan, E. Hemesath, L. Lauhon, Y. Rosenwaks, *Nano Lett.* **2011**, *11*, 183.
[43] P. Gruenbaum, R. King, R. Swanson, *J. Appl. Phys.* **1989**, *66*, 6110.
[44] M. Foldyna, L. Yu, P. R. I. Cabarrocas, *Sol. Energy Mater. Sol. Cells* **2013**, *117*, 645.
[45] K.-T. Park, H.-J. Kim, M.-J. Park, J.-H. Jeong, J. Lee, D.-G. Choi, J.-H. Lee, J.-H. Choi, *Sci. Rep.* **2015**, *5*, 12093.
[46] H. Malmbekk, L. Vines, E. Monakhov, B. Svensson, *J. Appl. Phys.* **2011**, *110*, 074503.
[47] H. D. Um, I. Hwang, N. Kim, Y. J. Yu, M. Wober, K. H. Kim, K. Seo, *Adv. Mater. Interfaces* **2015**, *2*, 1500347.

**ADVANCED
ENERGY
MATERIALS**

Supporting Information

Surface Passivation and Carrier Collection in {110}, {100} and Circular Si Microwire Solar Cells

Yun Goo Ro, Renjie Chen, Ren Liu, Nan Li, Theodore Williamson, Jinkyoung Yoo, Sangwan Sim, Rohit P. Prasankumar, and Shadi A. Dayeh*

Supporting Information

Surface Passivation and Carrier Collection in {110}, {100} and Circular Si Microwire Solar Cells

Yun Goo Ro, Renjie Chen, Ren Liu, Nan Li, Theodore Williamson, Jinkyoung Yoo, Sangwan

Sim, Rohit P. Prasankumar and Shadi A. Dayeh*

Y. G. Ro, R. Chen, R. Liu and Prof. S. A. Dayeh
Integrated Electronics and Biointerfaces Laboratory
Department of Electrical and Computer Engineering, University of California San Diego, La Jolla, California 92093, USA

Dr. N. Li, Dr. T. Williamson, Dr. J. Yoo, Dr. S. Sim, Dr. R. P. Prasankumar
Los Alamos National Laboratory, Los Alamos, New Mexico 87545, USA

Prof. S. A. Dayeh, Materials Science and Engineering Program and Department of NanoEngineering, University of California San Diego, La Jolla, California 92093, USA
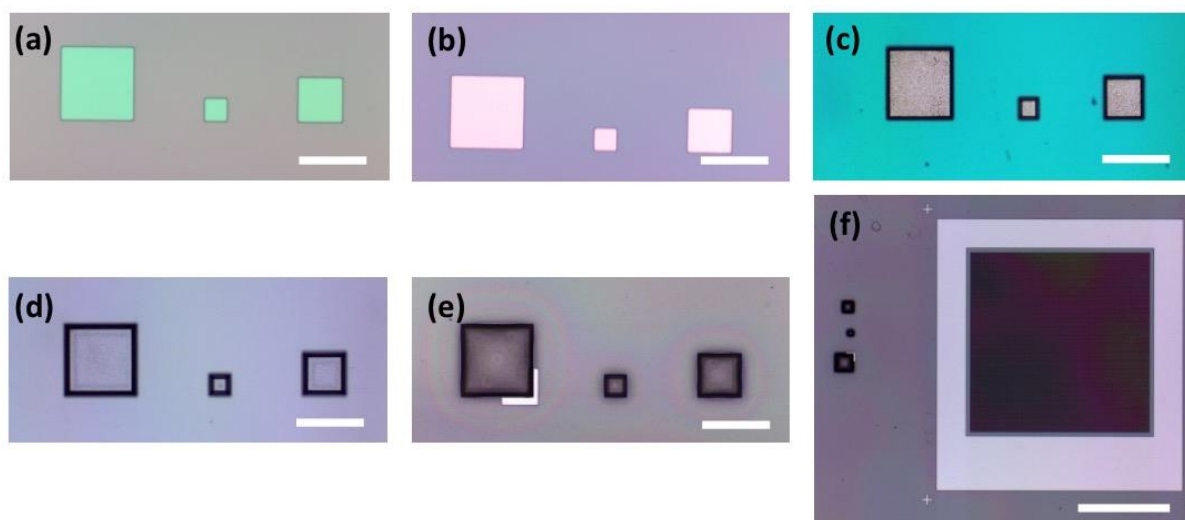
* E-mail: sdayeh@eng.ucsd.edu.

Figure S1. Optical microscopic images showing process flow of alignment of {110} flat-faceted Si microwire (SiMW) array by KOH etching. (a) Hard mask window patterning on SiN_x layer deposited on Si(100). (b) Hard mask window opening. (c) After KOH etching. (d) SiN_x mask removal. (e) Alignment mark patterning. (f) {110} flat-faceted SiMWs aligned in <110> direction. Scale bars are 100 μm for (a)-(e) and 500 μm for (f).
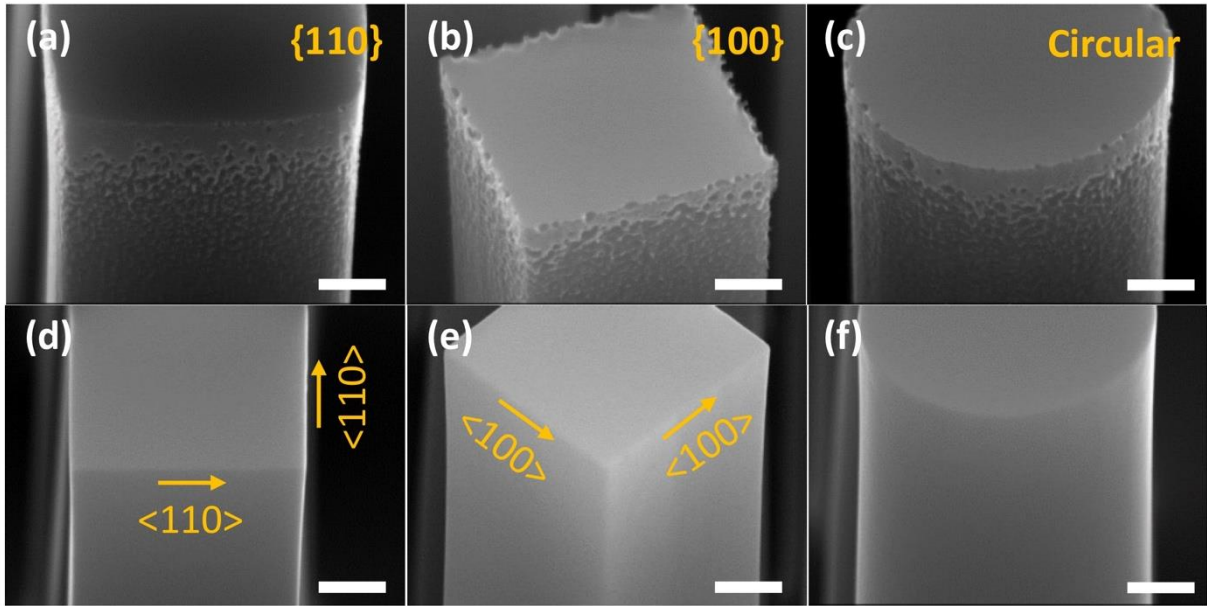
Figure S2. Magnified SEM images (45-degree view) of SiMWs with different facet orientations. (a)-(c) After ICP-RIE etching and Ni mask removal. (d)-(f) After thermal oxidation and strip. Scale bars are 500 nm.

Table S1. The average for measured solar cell performances from 3 runs for planar and SiMW solar cell devices with different facet orientations, without and with a surface passivation layer.

| Facet Orientation	J_{sc} [mA/cm^2]	V_{oc} [V]	FF [%]	η [%]
{110}, w/o	28.5±3.31	0.521±0.019	75.5±6.48	11.1±1.02
{110}, with	34.8±3.36	0.540±0.008	77.3±0.58	13.5±1.08
{100}, w/o	28.4±3.64	0.525±0.014	74.6±5.00	11.0±0.56
{100}, with	34.2±2.81	0.539±0.007	78.6±0.72	13.8±0.75
Circular, w/o	29.2±2.69	0.524±0.016	74.9±5.49	11.4±0.50
Circular, with	34.7±2.34	0.538±0.008	77.8±0.38	14.0±0.81
Planar, w/o	19.1±3.69	0.523±0.016	78.0±4.10	7.75±0.85
Planar, with	27.0±1.37	0.555±0.006	76.4±0.79	11.4±0.56
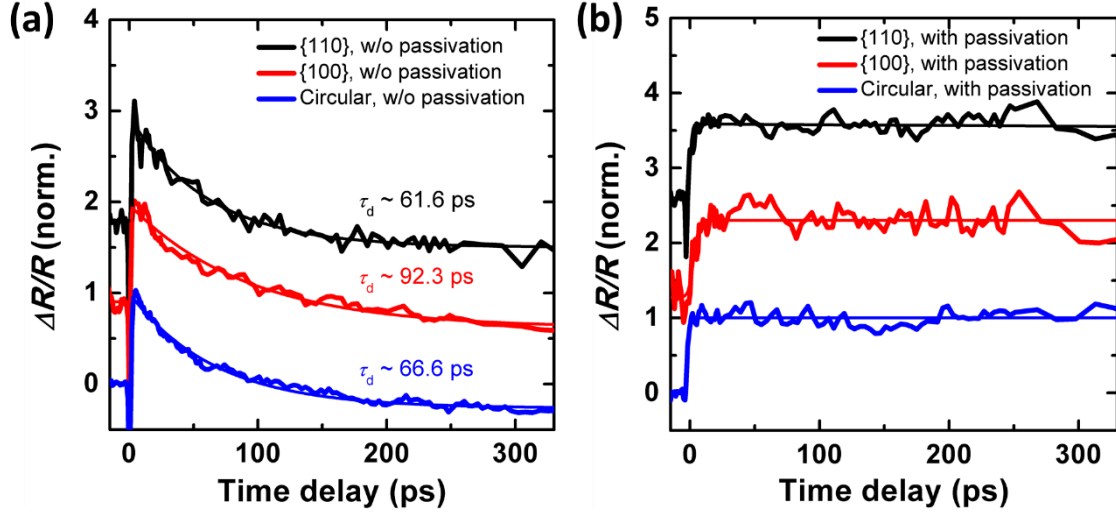
Figure S3. Ultrafast pump-probe measurements on (a) un-passivated and (b) passivated SiMWs with different facet orientations. Thick lines are measured normalized differential reflectivity ($\Delta R/R$) traces, offset for clarity. τ_d is the decay time constant, deduced from single-exponential fits (thin lines) to the traces.

τ_d for un-passivated SiMWs shows the longest lifetimes for {100} faceted SiMWs (92.3 ps) which agrees to our expectation that the {100} facet will have the lowest surface recombination due to its low surface state density. This also explains the higher Voc measured for un-passivated {100} faceted SiMWs as compared to that of un-passivated {110} and circular SiMWs. When a passivation layer (SiO$_2$/SiNx) is applied to SiMWs, the resulting time-resolved dynamics exhibited an extremely slow decay time that is beyond our measurement time range of ~300 ps, indicating that passivated SiMWs have a substantially longer minority carrier lifetime than un-passivated SiMWs, owing to reduced recombination from the passivated surface. Our ultrafast pump-probe microscopy setup[1] is based on a Ti:sapphire laser oscillator centered at 780 nm, the output of which is split into two arms. One arm is used as the probe and another arm is frequency-doubled in a BBO crystal to generate pump pulses at 390 nm. By using a 50X objective lens, the pump (2 μm spot size) and probe (1 μm spot size) beams are focused on an isolated single SiMW on a double-side-polished sapphire substrate. The polarization of both pump and probe beams are parallel to the SiMW axis. The initial carrier density generated by the pump is estimated to be $FA/E_{ph}d \sim 10^{18}$ cm^{-3},

where F = 430 µJ/cm^{-2} is the pump fluence, $A \sim 90\%$ is the absorbance of the SiMWs, E_{ph} = 3.18 eV is the pump photon energy and $d \sim 2$ µm is the SiMW diameter.
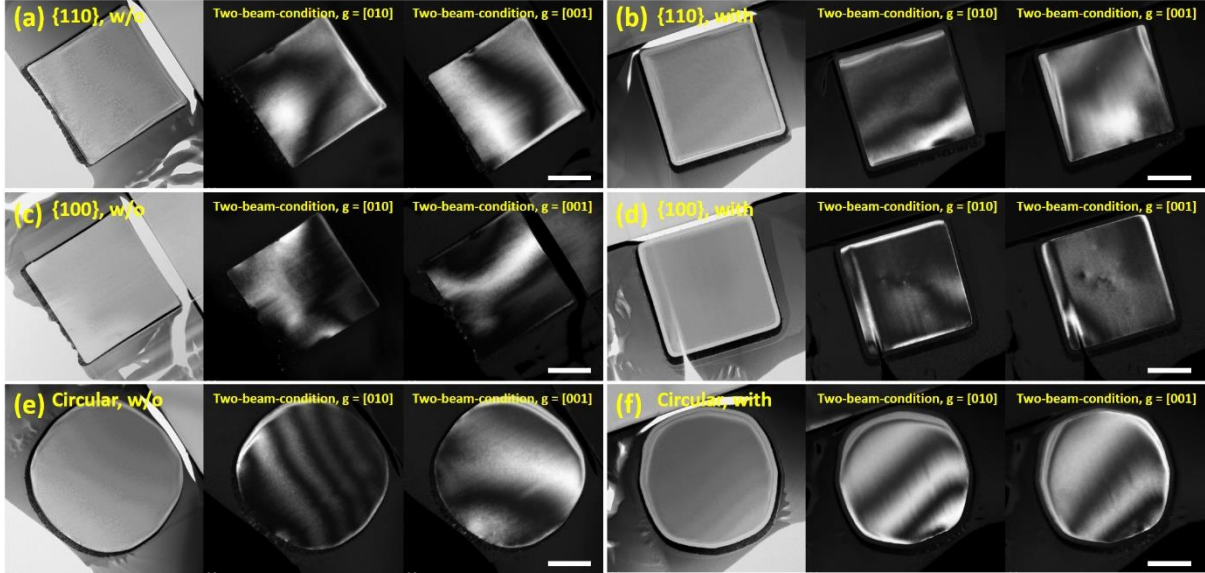

Figure S3. TEM images of SiMWs with different facets; bright field and dark field at two-beam conditions. Scale bars are 500 nm. Defects observed in the two-beam condition of (d) were induced during zone alignment.
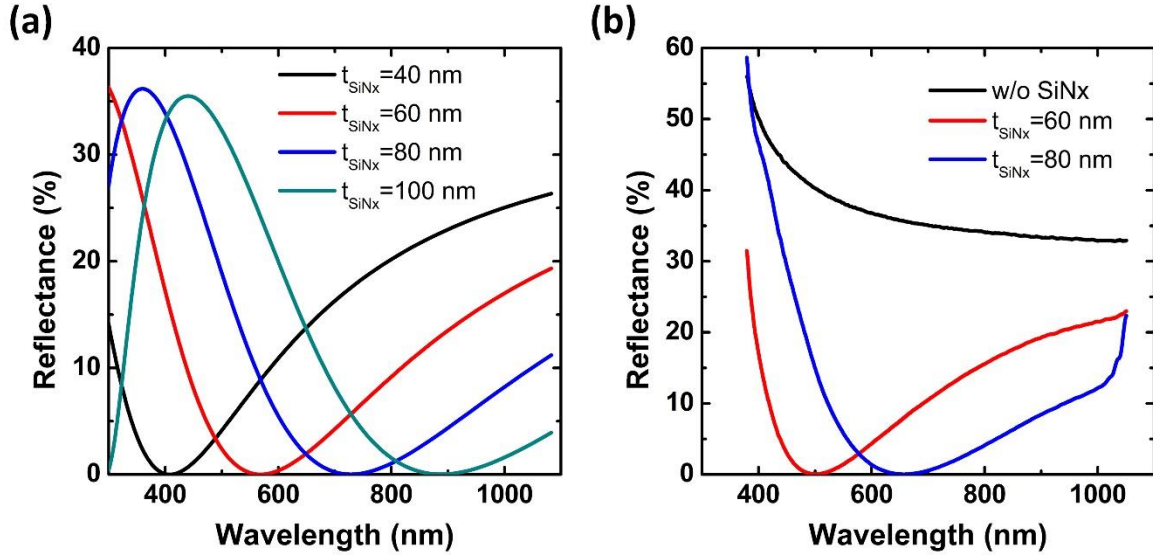

Figure S5. (a) Simulated and (b) measured reflectance of Si covered by SiO$_2$ (t_{SiO2}=10 nm) and SiN$_x$ layer with different thicknesses. Simulation was conducted using COMSOL Multiphysics.
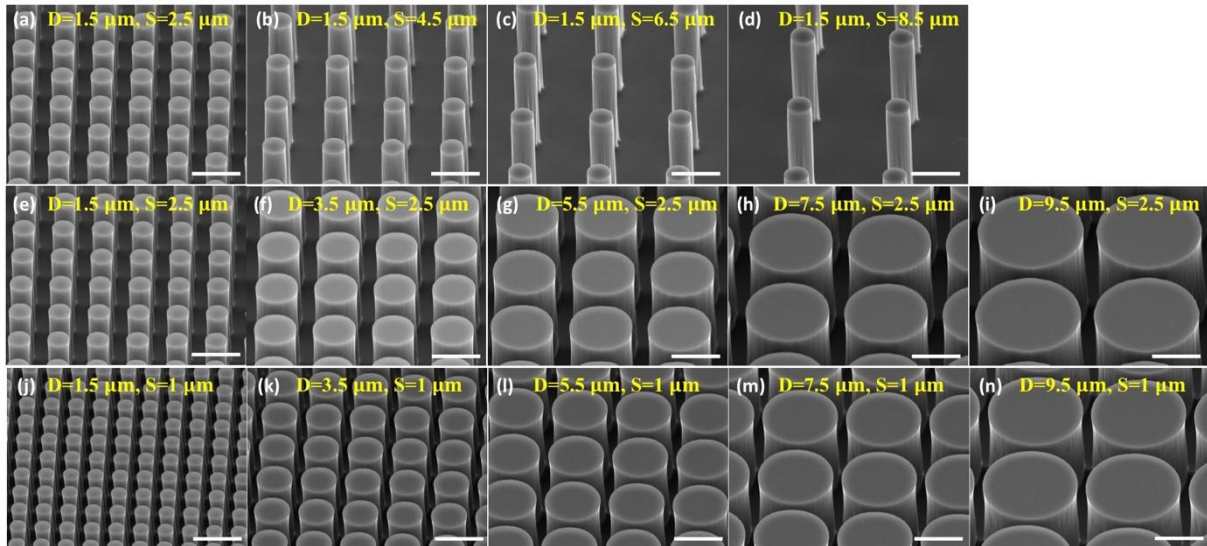
Figure S6. SEM images (45-degree view) of 10 μm-tall SiMWs with different *S* and *D*. Scale bars are 5 μm.

Table S2. The average for measured SiMW solar cell performances from 6 different runs of cells with different *S* (*D*=1.5 μm)

Device (*D*=1.5 μm)	J_{sc} [mA/cm^2]	V_{oc} [V]	*FF* [%]	η [%]
S=2.5 μm	30.9±1.98	0.540±0.005	77.8±1.02	12.8±1.00
S=4.5 μm	29.1±1.42	0.548±0.003	76.9±1.04	12.1±0.56
S=6.5 μm	28.4±1.05	0.547±0.007	76.2±0.69	11.5±0.67
S=8.5 μm	28.0±1.54	0.547±0.007	78.1±1.02	11.2±0.55
Planar	27.0±1.37	0.555±0.006	76.4±0.79	11.4±0.56

Table S3. The average for measured SiMW solar cell performances from 4 different runs with different *D* (*S*=1 μm).

Device (*S*=1 μm)	J_{sc} [mA/cm^2]	V_{oc} [V]	*FF* [%]	η [%]
D=1.5 μm	29.7±1.92	0.533±0.012	76.1±1.99	12.1±1.10
D=3.5 μm	30.0±1.54	0.534±0.009	77.4±1.53	12.1±1.26
D=5.5 μm	29.5±1.43	0.538±0.010	75.8±1.04	12.1±0.82
D=7.5 μm	29.3±1.33	0.537±0.011	76.3±1.56	12.0±1.01
D=9.5 μm	28.8±1.72	0.537±0.012	77.1±0.61	12.1±1.22
Planar	26.4±3.53	0.547±0.010	77.4±1.48	11.2±1.42

Table S4. The average for measured SiMW solar cell performances from 3 different runs with different top contact designs (*D*=1.5 μm, *S*=1 μm).

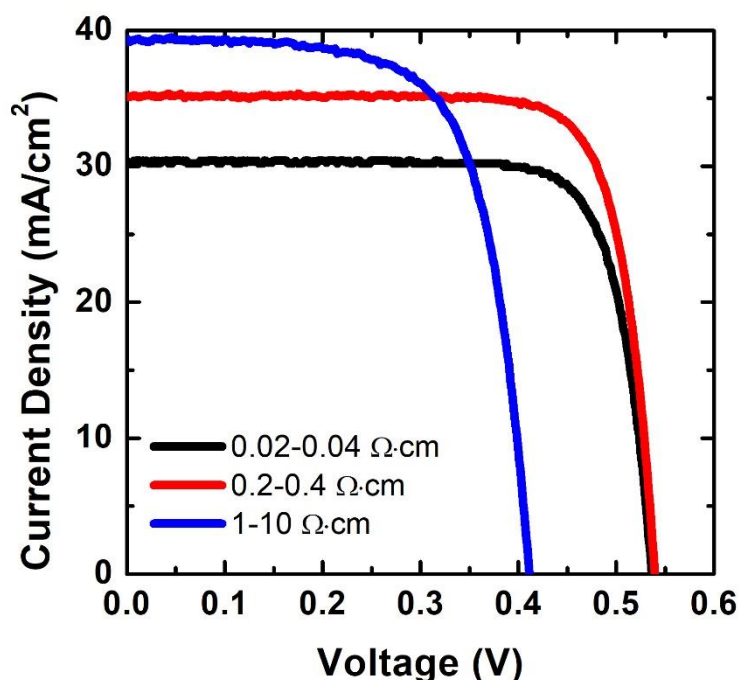| Device	Spacing of Adjacent Electrodes [μm]	J_{sc} [mA/cm^2]	V_{oc} [V]	*FF* [%]	η [%]
No mesh	980	29.4±2.56	0.533±0.014	77.4±1.44	12.1±1.31
2x2	490	29.3±4.64	0.532±0.014	76.7±1.56	11.9±2.20
3x3	320	29.6±4.76	0.532±0.015	77.1±1.97	12.2±2.52
4x4	235	29.7±4.78	0.533±0.015	77.8±2.14	12.4±2.59

Figure S7. Measured light *J–V* characteristics of Si planar cells with different substrate resistivities.

Table S5. Measured solar cell performances of Si planar cells with different substrate resistivities.

Base Resistivity of p-Si substrate [$\Omega \cdot$ cm]	Corresponding Carrier Concentration [atoms/cm^3]	J_{sc} [mA/cm^2]	V_{oc} [V]	FF [%]	η [%]
0.02 – 0.04	$9.1 \times 10^{17} – 2.7 \times 10^{18}$	30.4	0.537	79.2	12.9
0.2 – 0.4	$4.1 \times 10^{16} – 9.6 \times 10^{16}$	35.1	0.539	79.0	15.0
1 – 10	$1.3 \times 10^{15} – 1.5 \times 10^{16}$	39.4	0.411	68.7	11.1

Table S6. Measured solar cell performances of Si planar cells under different doping parameters. Base resistivity of *p*-Si substrate is 0.2 – 0.4 Ω ·cm.

Doping Parameters (Temperature, Time)	Emitter Sheet Resistance [$\Omega/\square$]	J_{sc} [mA/cm^2]	V_{oc} [V]	FF [%]	η [%]
925 ^{o}C, 10 s	160	33.7	0.541	75.7	13.8
950 ^{o}C, 10 s	120	33.7	0.555	77.0	14.4
950 ^{o}C, 15 s	101	31.8	0.546	73.8	12.8
950 ^{o}C, 20 s	88.5	32.7	0.537	75.6	13.3
975 ^{o}C, 10 s	93.1	32.6	0.531	68.3	11.8
975 ^{o}C, 20 s	64.6	34.0	0.545	74.6	13.8
1000 ^{o}C, 10 s	62.7	33.5	0.546	75.2	13.7
1000 ^{o}C, 20 s	47.9	32.6	0.541	66.3	11.7

The doping concentration and the junction depth of the emitter are determined by the doping temperature and time where the increase in temperature leads to an increase in both

6

surface doping concentration and junction depth while the increase in time results in increased junction depth but decreased surface doping concentration.[2,3] We optimized the doping concentration and the thickness of the emitter layer by comparing performances of solar cells that were fabricated under different doping temperatures and times to obtain optimal doping concentration and junction depth. From the results listed in Table S6, we concluded that a doping temperature of 950°C for 10 s to be the optimal conditions and were used as the fixed doping parameters for all cells that were reported here.

Estimation of external quantum efficiency and internal quantum efficiency

External quantum efficiency (*EQE*) was estimated using the following equation,

$EQE = (R_\lambda/\lambda) \times (1240 \text{ nmWA}^{-1}) \times 100\%$ where R_λ is the photoresponsivity [W^{-1}A] at a given wavelength of incident light and λ is the wavelength [nm].

Internal quantum efficiency (*IQE*) was estimated using the following equation,

$$IQE = EQE(1 - R)$$

where R is the reflectance. Here we assume that transmission through the substrate is negligible due to presence of the Al layer on the backside of the devices.

References

[1]   M. Seo, J. Yoo, S. Dayeh, S. Picraux, A. Taylor, R. Prasankumar, *Nano Lett.* **2012**, 12, 6334.

[2]   D. Mathiot, A. Lachiq, A. Slaoui, S. Noël, J. Muller, C. Dubois, *Mater. Sci. Semicond. Process.* **1998**, 1, 231.

[3]   U. Hashim, T. Adam, S. Fatimah, *J. Appl. Sci. Res.* **2012**, 8, 1154.